IN-SITU FIELD BIOFILM DETECTION USING SEISMIC METHODS

By

SUNDEEP SHARMA

Bachelor of Sciences in Environmental Sciences

New Jersey Institute of Technology

Newark, New Jersey

2012

Submitted to the Faculty of the
Graduate College of the
Oklahoma State University
in partial fulfillment of
the requirements for
the Degree of
MASTER OF SCIENCE
December, 2016

IN-SITU FIELD BIOFILM DETECTION USING

SEISMIC METHODS

Thesis Approved:

Estella Atekwana

Chair

Priyank Jaiswal

Javier Vilcaez

ACKNOWLEDGEMENTS

First and foremost, I would like to thank my committee: Dr. Estella Atekwana (chair), Dr. Priyank Jaiswal (Adviser) and Dr. Javier Vilcaez (Member) for their continued technical support throughout my time at Oklahoma State University. Secondly, I acknowledge funding from Chevron Energy Technology Company (Grant # CW852844). I also acknowledge Jason Masoner of the United State Geological Survey, Oklahoma City, OK for providing site access.

I would like to thank all the administrative bodies and faculties of the Boone Pickens School of Geology (BPSoG). It is their support and encouragement that has made this thesis possible. I would also like to thank all the friends and colleagues at BPSoG. Their friendship and support got me through toughest of times.

Lastly, I would like to thank my parents without whom none of this would have been possible. Their encouragement throughout my graduate career has been truly magnificent.

Name: SUNDEEP SHARMA

Date of Degree: DECEMBER, 2016

Title of Study: IN-SITU FIELD BIOFILM DETECTION USING SEISMIC METHODS

Major Field: GEOLOGY

Abstract: Biofilms are ubiquitous in subsurface environments and are being used in a variety of engineering and remediation applications. Their ephemeral nature makes them hard to detect and, as a result, the much needed *in-situ* imaging of their growth and distribution in time and space has remained a challenge. Laboratory studies have suggested that seismic waves, both Pressure (P) and Shear (S) modes of propagation, are sensitive to biofilm distribution but such observations have not been put to use in field settings till date. In this proof-of-concept study, use of surface seismic methods in detecting biofilms *in-situ* in field settings is demonstrated using a landfill site in Norman, Oklahoma, as an example. The experiment is to invert transmission and ground-roll waveform acquired along a 130 m long profile. Results show 50-60% increase in S-wave velocity and ~80% increase in P-wave attenuation within the water table oscillation zone. Environmental scanning electron microscope along with X-ray Diffraction images of soil samples from various depths affirms that presence of biofilms and not mineralogy sets the water table oscillation zone apart from the background. This finding is also consistent with sonic experiments in laboratories simulating biofilm growth in transitional environments. This paper further shows that a simple mechanistic model of biofilms coating quartz grains explains the anomalous increase in S-wave velocity due to presence of biofilms. Our results may be applicable to remotely detecting biofilms in biogeochemical hot zones (such as hyporehic zone, contaminant plume fringe and groundwater fluctuation zone), soil remediation, biobarriers, microbial enhanced oil recovery, and carbon sequestration studies.

TABLE OF CONTENTS

LIST OF TABLES

LIST OF FIGURES

Figure Page

CHAPTER I

INTRODUCTION

In subsurface environments microorganisms have the tendency to attach to surfaces of sediment grains and develop biofilms, consisting of extracellular polymeric substances (EPS) (*Tsuneda et al., 2003*). The EPS play a significant role in determining the overall biofilm architecture as well as adhesion to the growth surface; but can also lead to clogging of a porous medium with attendant changes in the effective porosity and hydraulic conductivity (*e.g., Taylor and Jaffe 1990; Cunningham et al., 1991; Vandevivre and Baveye 1992; Baveye et al., 1998; Hand et al., 2007; Seifert and Engesgaard, 2007 and references therein)* causing the development of preferential flow paths (*e.g., Seifert, 2005*). Biofilm clogging of porous media has been harnessed for a variety of field bioengineering applications such as soil improvement and remediation (*DeJong et al., 2010*), formation of bio-barriers (*Kao et al., 2001*) groundwater remediation (*Kasi et al., 2011*), CO2 sequestration (e.g., *Mitchell et al., 2010*), and microbial enhanced oil recovery (MEOR) (e.g., *Lazar et al., 2007*). Yet, how spatiotemporal response of biofilm growth to changes in ambient conditions in the above experiment is not well known because of the lack of proper *in-situ* field detection and monitoring techniques.

Monitoring of bioclogging in laboratory setting has been very successful and, to date, a variety of microscopy techniques have been demonstrated successfully. These include confocal laser scanning microscopy (*DeLeo and Baveye, 1997; Leis et al., 2005; Rodriguez and Bishop, 2007*), light microscopy (*e.g., Paulsen et al., 1997; Sharp et al., 2005; Yang et al., 2000*), plate counting (*Brough et al., 1997*), synchrotron-based X-ray computed microtomography (CMT) (*Iltis et al., 2011*), and tracer tests (*Sharp et al., 1998*). The biggest drawback of these methods is their invasive nature that has a potential to interfere with microbial growth, Further, these methods are only able to image a very limited area/volume and may not be abaptable to large-scale field investigations. In the last decade, researchers have also experimented with non-invasive geophysical methods such as ultrasonic *(Davis et al., 2009; 2010; Kwon and Ajo-Franklyn, 2013; Noh et al., 2016),* and induced-polarization signals (*Ntarlagiannis and Ferguson, 2008; Abdel Aal et al., 2010; Zhang et al., 2014*). Geophysical methods are non-interfering and have good spatial coverage but the data can be difficult to interpret due to coupled processes.

To date much of our information about biofilm growth in porous media is either based on laboratory experiments or numerical models that explain data from the laboratory tests (e.g, *Iltis et al., 2011*). Such information, although essential, is not adequate for controlling field applications. Field monitoring of biofilm growth is still in its preliminary stages involving simple methods such as tracer tests that provide elementary understand of pore clogging (*Seifert and Engesgaard, 2007*). To the best of our knowledge, there exists only one successful study till date, which conducted in a wellbore setting (essentially one-dimensional, 1D), demonstrated that the nuclear magnetic resonance tool can detect biofilm growth *in-situ* (*Kirkland et al., 2015*).

The field seismic method holds promises. It is known that biofilms generally tend to exist as an adsorbed phase on mineral grains or as suspensions in pore spaces (Cunningham 1991) and in either case, because biofilms are viscoelastic in nature (*Stoodley et al., 1999; Klapper et al., 2002; Ahimou et al., 2007*), they are likely to change the elastic moduli of their host sediments. Therefore, in principle, above a threshold saturation, biofilms should produce noticeable modulations in the seismic signals. This idea that was first demonstrated by Davis et al. (2009) by testing the effect of biofilm growth on compressional waveforms over a 29-day experiment. Davis et al. (2009; 2010) found that, in comparison to a background non-stimulated column, the amplitudes and arrival times of the acoustic wave from a biofilm-inoculated column changed in ways that could be correlated to the biomass growth. Although changes in waveform arrival times were subtle, waveform amplitudes from parts of the biostimulated column decreased by as much as up to ~80%. Later, Jaiswal et al. (2014), using a simple mechanistic model, showed how the Davis et al. (2009) waveform modulations could be explained by appropriating the biofilms between the two growth modes – biofilm becoming a part of pore fluids and biofilm becoming a part of sediment matrix.

In another experiment, using a different strand of bacteria and slightly different setup than Davis et al. (2009; 2010), Kwon and Ajo-Franklin (2013) also measured the compressional waveform modulation as well as permeability of a biostimulated column over a 20 day period. Similar to Davis et al. (2009), they also observed subtle changes in arrival times and up to 80% decrease in amplitudes. More importantly, they were able to show that biofilm growth changed the permeability of the host medium. More recently, Noh et al. (2016) were able to propagate both compressional and shear waveforms

through a stimulated column for 38 days. The attenuation behavior (amplitude decay) in both kinds of waves were similar; compressional and shear waveforms had a peak attenuation of ~80% and ~60% respectively. However, as opposed to the compressional-wave arrival-times, which showed only subtle changes in the experiment, the shear-wave arrival-times decrease by more than 50%. Why shear-wave velocity (V_S) should increase so much more than the compressional-wave velocity (V_P) has not been adequately explained by any research team till date.

Although the causative relation between biomass distribution and waveform modulation is not clear, the laboratory studies affirm that seismic methods have the potential to detect biofilms in porous media. In this paper, we advance the science of biofilm monitoring and detection by testing the potential of surface seismic technique at an appropriate field location. Although the host medium and nutrient supply in our case is vastly different from the laboratory studies that provide impetus for this study, the physical principles that underlie seismic waveform modulations by biofilms, should remain the same. In the end, we also explain our (and possibly that of Noh et al., 2016) results though a simple mechanistic model. The potential of imaging microbial process through surface seismic methods offers a ready deployable minimally-invasive approach for quantifying subsurface microbial processes benefiting soil engineering, groundwater remediation, CO2 sequestration, and microbial enhanced oil recovery (MEOR).

CHAPTER II

STUDY SITE

The Norman landfill site is a closed municipal solid waste landfill site located south of the city of Norman, Oklahoma and overlies alluvial deposits of the Canadian River (Figure 1). Since 1995 the United States Geological Survey (USGS) has classified this site as a part of the Toxic Substance Hydrology Program and began extensive investigation. This site received solid waste dumped into trenches about 3 m deep beginning in 1922 and had no restrictions in terms of the kind of materials that could be dumped. The practice then was to cover a layer of solid waste with 15 cm thick layer of sand before laying the next layer of waste. Waste handling methods were modified in late 1970's and early 1980's and, finally, in 1985, under the Resource Conservation and Recovery act (RCRA), the site was closed.

The geology beneath the study site consists of 10-12 m thick fine-to-medium grained sand and discontinuous layers of silt, classified as the Canadian River alluvium. The base of this alluvium layer consists of a high hydraulic conductivity coarse sand and gravel layer (*Collins 2001*). The top of the water table at the Norman Landfill site fluctuates between 1 m and 3 m in response to seasonal evapotranspiration and rainfall (Scholl et al., 2004). Precipitation along with the groundwater flow has created a leachate

plume from the landfill that appears to be growing and migrating towards the Canadian River (*Cozzarelli et al 2001*). For example, the leachate plume (yellow polygon in Figure 1) has been expanding from an area of 20,800 m^2 to 203,400 m^2 (almost ten times) between the years 1986 to 2010 (Masoner and Cozzarelli, 2015).

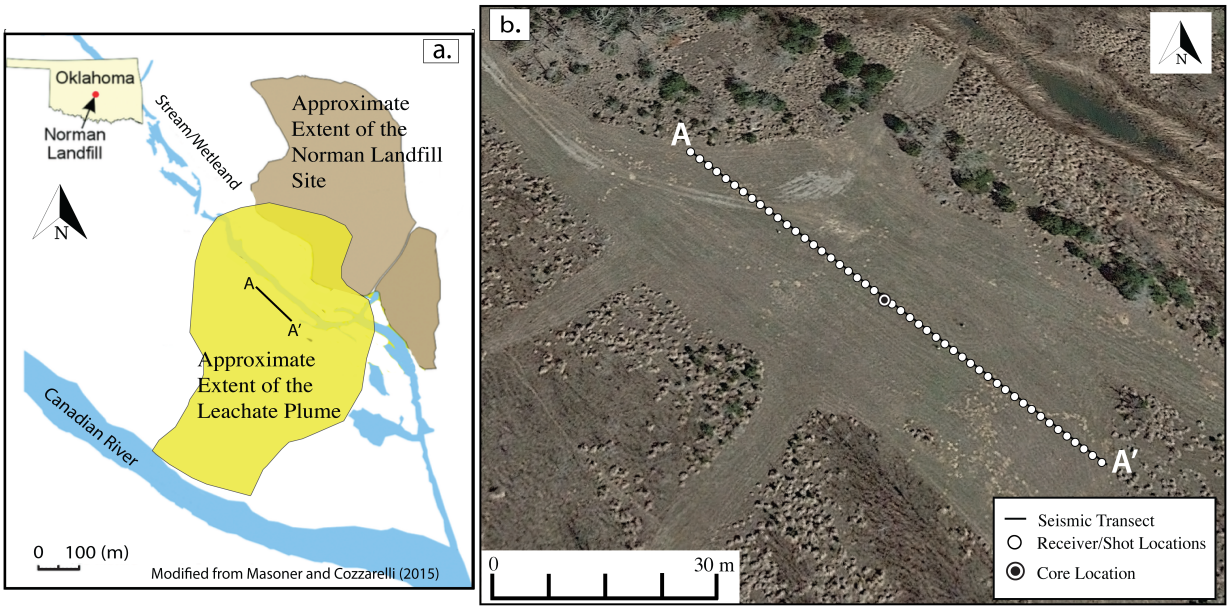

Figure 1 *– Study site. a) Map of the Norman landfill site (modified from Masoner and Cozzarelli, 2015). Yellow polygon indicates the approximate extent of the leachate plume. Brown polygons indicate approximate extent of the landfill site. Seismic profile, A-A', is labeled. b) Arial photograph of the acquisition area. Solid white dots indicate the coincident shot-receiver locations. Solid black dot indicates the core location.*

Geochemical and microbiological data acquired by the USGS in the last decade at the site has shown that iron reduction, sulfate reduction and methanogensis are the main terminal electron processes, creating concentration gradients within the top 10 m of the subsurface. Cozzarelli et al. (2011) observed significant influence of temporal hydrological processes in controlling chemical concentrations at the plume boundaries. In particular, Cozzarelli et al. (2011) also found that redox reactions were most active at the top of the plume probably due to seasonal recharge.

CHAPTER III

METHODS

Our seismic profile is located in the central part of the leachate plume southwest of the main landfill location (Figure 1). The flat topography along the profile helps in minimizing the arrival time uncertainties from elevation statics. The profile was acquired using 48 receivers and co-located sources spaced 2.7 m apart. The geophones were vertical component with resonance frequency of 10 Hz. The sources were point explosives comprising a shotgun and 400–grain 8–gauge blank shells. Sample interval of the field data was 0.125 ms and trace length was 500 ms. The raw data had low random noise but strong low-frequency and high-amplitude Rayleigh waves (red box – Figure 2). The transmission coda was also string and the seismic energy could be clearly seen up to the farthest offsets on all shots (blue box – Figure 2). No prominent reflection or diffraction arrivals could be identified within 250 ms. Our acquisition did not use horizontal sensors and therefore the SH-propagation model was not directly recorded which limited ways in which V_S could be estimated. Fortunately, the strong Rayleigh waves (which dominantly make up the ground roll cone) allowed us to indirectly estimate the V_S. Estimating V_P (and the corresponding attenuation; Q_p^{-1}, where Q is commonly

known as the seismic quality factor) was rather straightforward, by inverting the compression coda under visco-acoustic approximations.

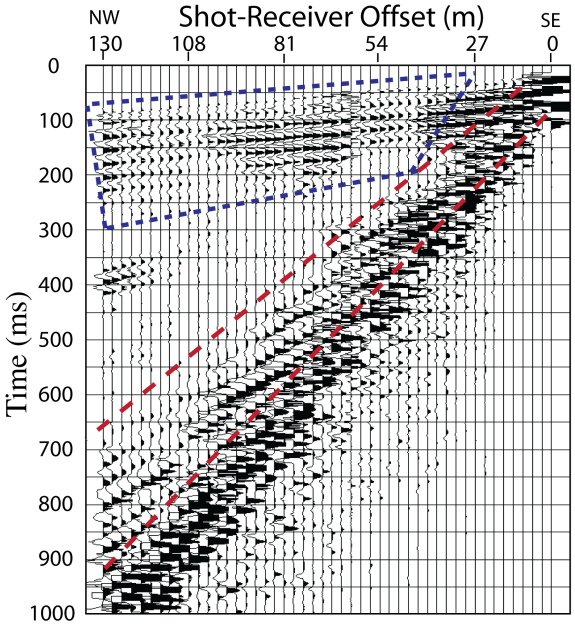

Figure 2 *– a) Data from the south-easternmost shot. The transmission and the Rayleigh wave data respectively inverted for P-* and S-wave velocities (*V_P and V_S respectively) are enclosed within blue and red dashed polygons. Shot located at model distance 130 m in Figure 3.*

To estimate V_S from Rayleigh wave coda we have used a method proposed by Xia et al. (1999), commonly referred to as the Multichannel Analysis of Surface Waves (MASW). We provide a brief summary of this method below and point the reader to the original references for details. The Xia et al. (1999) method assumes that the dominant signal in a seismic gather is ground roll itself. Therefore, to prepare our field data for MASW we applied a general bandpass filter of 10-20-60-120Hz. The key in Xia et al. (1999) method is that every frequency of the Rayleigh-wave propagation mode has a unique velocity (known as its phase velocity) but the move-out (change in arrival time

with increasing source-receiver separation) is linear. Thus, when individual mono-frequency gathers obtained through Fourier transform of the time-domain field data are stacked into a single-trace for a range of move-out velocities, the energy of the stack (summation of the square of the amplitudes) increases as the stacking velocity approaches the propagation velocity of that particular frequency. The stacked energy for a range of combinations is displayed as a cross-plot between phase-velocities and frequencies. A velocity-frequency function, also known as dispersion curve (Figure A1), is then interpreted by the user solely based on the semblance structure of the cross-plot. Prior to the stacking, the energies between individual mono-frequency gathers are balanced through amplitude normalization. To compensate for time delay for a specific offset, an offset-dependent phase shift is also applied as needed.

Physically, the Rayleigh-wave phase velocities (c_R) are a function of material properties such as V_S, V_P and bulk density (ρ). Of these, at frequencies higher than 5Hz, V_S influences c_R much more than V_P or ρ (Xia et al., 1999). In a modeling sense, if V_S is the model vector (**m**) and c_R is the data vector (**d**), they can be related as:

$$\mathbf{J}\Delta\mathbf{m} = \Delta\mathbf{d}, \qquad (1)$$

where, **J** is the Jacobian (Equation 2), $\Delta\mathbf{d}=\mathbf{d}_{obs}-\mathbf{d}_{pred}$, data error, is the difference between observed and the predicted data vectors and $\Delta\mathbf{m}$ is the update vector also known as model roughness. The Jacobian is expressed as:

$$\boldsymbol{J} = \left[\frac{\delta F/_{\delta V_{si}}}{\delta F/_{\delta C_R}}\right] \quad , \qquad (2)$$

where F is a nonlinear function of frequency, c_R, V_S, V_P, ρ, and thickness of the layer (h) for which the material properties are being defined. The model parameterization is done

assuming a layered earth. Equation (1) is solved for the model vector in an inverse sense by defining an objective function, $\mathbf{E^{RW}}$, as an L_2 norm of the combination of data errors and model roughness, and minimizing it in a least-square sense.

$$E(m) = \Delta \boldsymbol{d}^T \boldsymbol{W} \Delta \boldsymbol{d} + \Delta \boldsymbol{m}^T \alpha \Delta \boldsymbol{m} \quad (3)$$

In Equation (3), $\mathbf{W}$ is a weighting matrix, based on differences in c_R with respect to frequency, and α is the damping factor, introduced for solution stability, to serves as a tradeoff between model roughness and data errors (Donald W. Marquardt, 1963). The inverse problem is solved iteratively with the help of a staring model, $\mathbf{m_0}$, which is an initial guess of the layer-cake subsurface structure. In each iteration, the damping factor is reduced so that the solution is dictated more by the data errors and less by model roughness. Reduction of data errors over successive iterations is indicative of the inverse problem converging to a solution. The halting criterion is implemented by either a fixed number of iterations or setting a tolerance for α. Xia et al. (1999) proposed the singular value decomposition as an efficient method of minimizing Equation (3). A salient aspect of this method is that although $\mathbf{m_0}$ is formulated in terms of V_S, V_P, ρ, and h, the inverse only solves for V_S. Other parameters are updated proportionally. As nominally expected, the sensitivity of c_R to V_S is depth dependent, i.e. lower frequencies penetrate deeper. Further, V_S solution from Rayleigh wave inversion is 1D.

Our profile was acquired using a static array, i.e., all receivers recorded all the shots. Therefore, to obtain a comparable dispersion curves from one location to another, we regrouped the traces. Instead of assuming that every receiver records every shot, only a fixed number of traces (up to a predetermined offset trailing the shot) were assigned to every shot. This converted the static acquisition gets into the roll-along type, where a

moving source is followed by a fixed number of receivers. The maximum offset (source-receiver separation) for the roll-along geometry was determined in a trial-and-error manner such that the fundamental mode dispersion has high energy in all records being used for analysis. We found that a receiver spread of 10 geophones provided the widest frequency bandwidth (10 – 100 Hz) and with highest signal-to-noise ratio. Using this, the static array was decomposed into 38 roll-along shot gathers assuming that the shots were moving from southeast to northwest. Equal numbers of gathers could be created in the reciprocal direction as well. Since inversion of individual shot records creates a single 1D V_S profile located at the center of the spread length, for best results, two V_S models from reciprocal roll-along surveys occupying at the same ground locations were averaged. Therefore, the final V_S model is only being presented for locations between 30 m and 110 m model distance, which was common to both roll-along directions.

To estimate V_P and Q_P^{-1} from the transmission coda, we have inverted the arrival times followed by the full waveforms. For traveltime inversion we have used the Zelt and Barton (1998) algorithm and for the full-waveform inversion we have used the (Pratt, 1999) algorithm. A brief introduction to both methods are provided here, but the reader is guided to Zelt and Barton (1998) and Pratt (1999) for further details. Much like the previously described Rayleigh wave inversion, both these algorithms solve the non-linear inverse problem iteratively through a local decent method with the help of the starting model. Since the solution from both these inversion algorithms is 2D, the staring model is defined on a finite-difference grid. The model vector comprises only V_P for traveltime inversion and V_P and Q_P^{-1} for waveform inversion. The data vector for the traveltime inversion comprises the first arrival times and for the waveform inversion comprises the

Fourier coefficients (both frequency and phase spectrum) of the time domain data. Attenuation is included in the inversion by specifying the velocity model (**m**) as a complex quantity ($\mathbf{m} = \mathbf{m_r} + i\mathbf{m_i}$), where the imaginary ($\mathbf{m_i}$) and the real ($\mathbf{m_r}$) parts are related through the seismic quality factor Q, as:

$$m_i = -\frac{m_r}{2Q} \tag{4}$$

Traveltimes in the forward modeling part of the regularized Zelt and Barton (1998) algorithm are computed on a regular grid by solving the Eikonal equation using a finite difference scheme (Vidale, 1988). Raypaths, in accordance with Fermat's principle, are determined by following the steepest gradient of the time field from a receiver to a source. The forward modeling resembles the Vidale (1988) method modified to account for large velocity gradients (Hole and Zelt, 1995). The wavefield in the forward modeling part of the Pratt (1999) algorithm is computed by solving the wave equation in the frequency domain using a finite-difference scheme and a mixed-grid approach of (Jo et al., 1996). The Pratt (1999) uses an acoustic, isotropic approximation of the wave equation. Additionally, Gardner's relationship (Gardner et al., 1974) between density and velocity is assumed and attenuation is ignored (Brenders and Pratt, 2007). The Pratt (1999) algorithm also allows for calculation of Q_P^{-1} using the real and imaginary part of the complex velocities.

Although the overall approach of both the Zelt and Barton (1998) and Pratt (1999) inversion algorithms towards assuring a convergence are similar, formulation of the decent method and halting criteria are different. The traveltime inversion minimizes an objective function, $E(m)^{TT}$, that is the L_2 norm of a combination of data misfit and model

roughness (Equation 5). Whereas for the waveform inversion the objective function, $E(m)^{WV}$, is the L_2 norm of only the data errors (Equation 6). As a result, the traveltime inversion seeks a minimum-structure model that fits the observed traveltimes only to the level of their respective uncertainties, while the waveform inversion seeks a model that can explain as many features of the observed seismograms as possible within the range of the wavenumbers being accounted for. The input data for traveltime inversion are the first arrivals and in waveform inversion they are the frequencies.

$$E(m)^{TT} = \Delta \boldsymbol{d}^T \boldsymbol{C}_d^{-1} \Delta \boldsymbol{d} + \lambda [\boldsymbol{m}^T \boldsymbol{C}_h^{-1} \boldsymbol{m} + s_z \boldsymbol{m}^T \boldsymbol{C}_v^{-1} \boldsymbol{m}] \quad (5)$$

$$E(\mathbf{m}) = \frac{1}{2} \Delta \mathbf{d}^t \Delta \mathbf{d}^* \quad (6)$$

In Equation (5) $\boldsymbol{C}_d$ is the data covariance matrix (similar to **W** in Equation 3), $\boldsymbol{C}_h$ and $\boldsymbol{C}_v$ are model space covariance matrices that measure horizontal and vertical roughness, respectively, λ is the trade-off parameter (similar to the scaling factor in Equation 3), and s_z determines the relative importance of maintaining vertical versus horizontal model smoothness in model updates. The traveltime inversion is halted when the predicted times are within a predefined threshold of the observed arrival time. The threshold, which is the uncertainty in traveltime picking, reflects a combination of dominant frequency, ambient noise and source-receiver reciprocity.

In Equation (6), the superscript *t* represents matrix transpose, and the superscript * represents the complex conjugate. An important aspect of waveform inversion is its implementation using a multi-scale approach advocated by (Bunks, 1995) to mitigate its non-linearity. This approach of solving the inverse problem proceeds from low to high wavenumbers, using low temporal frequencies first and then refining the solution with

higher frequency data. Visual assessment of the updated model for its overall geological sensibility and the predicted data for their similarity to the recorded data serve as the stopping criteria in waveform inversion.

Prior to traveltime and waveform inversion, we preconditioned the field raw data to make them suitable for the application of the Zelt and Barton (1995) and Pratt (1999) algorithms. Both these algorithms assume that the subsurface is not elastic, i.e., no mode-conversion happens, and no free surface is present in the model. Therefore, we first muted the Rayleigh wave coda. Next, we suppressed high frequency random noise by applying a band pass filter of 16-30-60-120 Hz. Then, we picked the first arrival times for traveltime inversion on all shot gathers. As a clarification, gathers used for traveltime and waveform inversion corresponded to the static array. We assigned 1 ms uncertainty to the traveltime picks. The starting models for traveltime inversion was 1D in nature where velocities increased linearly with depth; from 1400 m/s at the surface to 1800 m/s at 10 m. This gradient is not arbitrary. It was determined heuristically through repeated tests. The model from every inversion run was averaged to create the starting *model* for the next test. Using this starting model, the inversion converged in 9 iterations.

We used the V_P solution from traveltime inversion as a starting model for waveform inversion, which is a standard practice. Data preconditioning for waveform inversion was somewhat rigorous. First, the effect of non-physical factors such as source-receiver directivity and inconsistent coupling were removed. For this, field gathers were bulk scaled using data simulated from the final traveltime V_P solution using a 10-100Hz minimum phase ricker wavelet. As a clarification, no amplitude-versus-offset (AVO) scaling was done at any stage of processing. Then, the scaled gathers were windowed in

time to only include the transmission coda (as opposed to additional deeper reflections) in waveform inversion. The window was 1s long with its top set at 10ms earlier than the first arrivals and cosine tapering at both ends (cosine tapering helps in minimizing the Gibbs phenomenon).

The lowest signal frequency in the field data was 32 Hz. As a first step in waveform inversion, we low-pass filtered the data to enhance the 32-40 Hz range and estimated an initial source signature by inverting 32, 36 and 40 Hz frequencies as a group. We used the estimated source signature for forward modeling to ensure that the first arrivals were within one half-cycle of their picked times, i.e., the starting model was correct. Then, we held the phase of the inverted source constant and updated the velocity model. This resulted in very broad and smooth model updates. Following this we moved to the next higher frequency bandwidth to update the source and velocity model. Instead of individual frequencies (say F) we inverted them in groups of three (F-4, F and F+4 Hz). Through repeated forward modeling and data comparison, we found that not all frequency groups led to meaningful updates, maybe due to varying noise content. After the 36 Hz group, we found inversion of 48 Hz, 68 Hz, 88 Hz and 128 Hz provided reasonable model updates. In every group, inversion was halted when reduction in misfit was less than 1%.

CHAPTER IV

RESULTS AND DISCUSSION

A 2D V_S model interpolated from the individual 1D profiles is shown in Figure 3a. We observe three distinct layers in the 2D V_S model; an upper layer (0-1.3 m depth) with velocities that range between ~90-110 m/s, an intermediate layer (1.3-3 m depth) with velocities ranging between ~150-180 m/s, and a low velocity bottom layer (3-4.5 m depth) with velocities ranging between ~80-110 m/s. Assuming the background velocity to be ~80-110 m/s, it implies that there is a 50-60 % increase in V_S within the intermediate zone. As V_S is not sensitive to fluid within the pores, the observed increase in this intermediate layer could relate to lithological changes. To provide further insight into the V_S increase within the intermediate layer, we plot the 8-year water-table fluctuation zone on our 2D V_S model (Figure 3a). Interestingly, the water table fluctuation zone bounds the intermediate high V_S layer. Studies have suggested the water table oscillation zones are biological hotspots where enhanced microbial activities (and biofilm formation) occur due to mixing of necessary nutrients (*Rijal et al., 2010; Atekwana et al., 2014, Borch et al., 2009; Totsche et al., 2010; Stegen et al., 2016*). In their laboratory experiment, Noh et al. (2016) also observed greater than ~50% increase in V_S due to

biofilm growth. We posit that the intermediate depth high V_S layer in Figure 3a is a microbially active zone.

To further examine the intermediate depth high V_S layer in Figure 3a we retrieved a core from the 70 m horizontal distance location. We present four representative Environmental Scanning Electron Microscope (ESEM) images of the sediment samples, S1 – 4, from different depths along the core (Figure 3b). Samples S1 and S4 are outside (above and below, respectively) the intermediate-depth high V_S layer. These samples do not show biofilms or any associated byproducts of microbial activities. Sample S2 and S3 are located at the top and bottom of the intermediate-depth high V_S layer respectively. Both samples clearly show biofilm coating and binding the mineral grains together. Thus there is strong evidence that the intermediate depth high V_S layer in Figure 3a is anomalous in terms of biofilm content. We used X-ray diffraction of samples from the same depths to affirm that the mineralogy throughout the core is very similar (99% quartz, data not shown). Therefore, it is very likely that the anomalously high V_S layer is due to the presence of biofilms. However, the biofilm is not as uniformly distributed within this layer as suggested by the model. Its uniform appearance occurs due to interpolation of a set of uniformly spaced 1D profiles. On a related note, the horizontal resolution of the model in Figure 3a is more than 10 m but its vertical resolution is as high as 0.5 m.

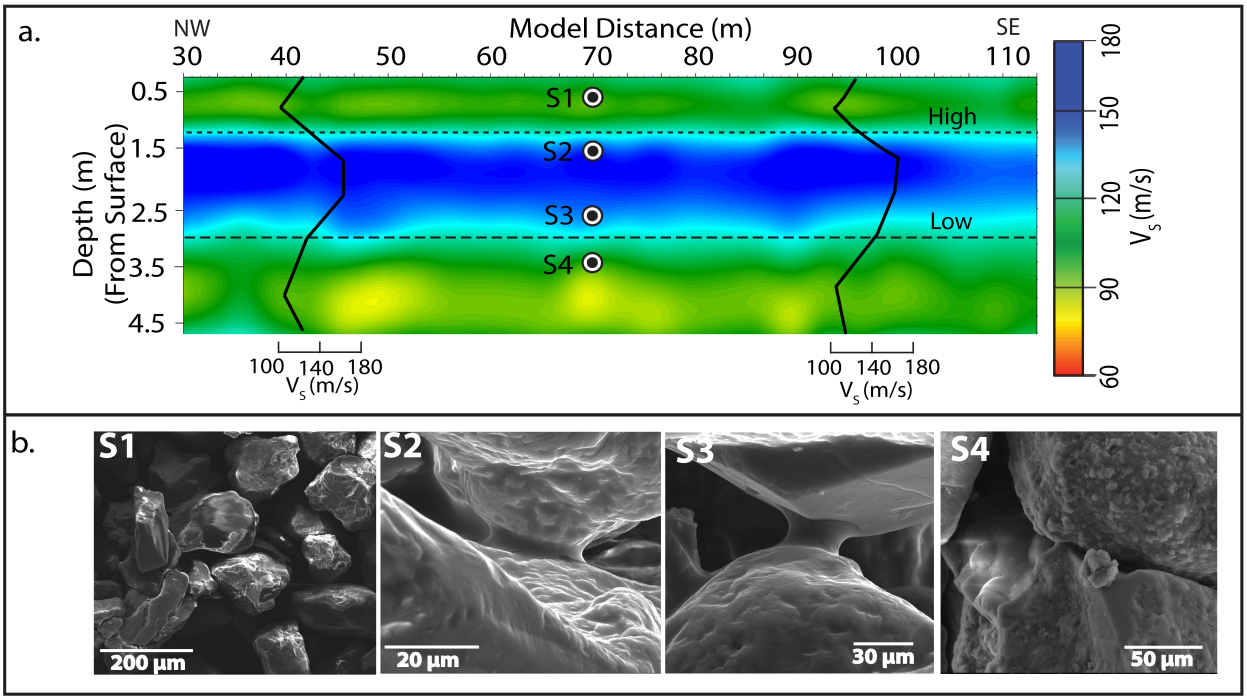

Figure 3– *a) V_S solution from Rayleigh wave inversion. Individual 1D V_S profiles generated at every 10m interval were interpolated to obtain this 2D section. Two representative 1D V_S profiles, at 40 m and 95 m model distance, are overlaid. Historic water table high and low bounding a water table oscillation zone is marked with dotted lines and labeled. Note the higher V_S within the oscillation zone compared to the background. Solid dots are locations of samples, S1 – S4, used for microscopy. b) Environmental scanning electron microspore (ESEM) images of samples S1 to S4. Samples, S1 and S4, outside the oscillation zone do not show biofilm while samples, S2 and S3, within the oscillation zone show biofilm.*

In their laboratory experiment, Noh et al. (2016) also considered the effect of biofilm formation on the V_P and Q_p^{-1}. They observed only a subtle change in the V_P (~2%) but a significant increase in the Q_p^{-1} (~50-80%) for sediments with ~9-10% biopolymer saturation. From inversion of the transmission data, we have two V_P solutions available to interpret. These solutions are, of course, at two different resolutions. The solution from traveltime inversion (Figure 4a) has a very smooth structure with no expressions of the water table oscillation zone. The solution from the waveform inversion (Figure 4b) has higher resolution but it also does not show any anomalous expression of the water table oscillation zone (Figure 4b). Minimal changes in V_P due to the presence of biofilm is

expected based on the laboratory studies of Davis et al., 2009 and Noh et al., 2016. On a related note, two zones with lower V_P, between 40 m and 60 m model distances are observed within 3 m depth (Fig. 4). The V_S solution (Figure 3a) did not show any anomalous values at these locations. Lower V_P with minimal changes in V_S can occur when free gas is present. At the study site microbial growth can produce free gas. Lower V_P can also result from subtle changes in soil composition and/or porosity.

Next, we solve for the Q_p^{-1} structure using the full-waveform inversion. We use the final V_P solution (Figure 4b) as the starting model for this effort. This is a nominal procedure which assumes that the first order amplitude variations in the data are due to optical focusing while the higher order variations are due to local energy loss. The starting Q_P^{-1} model assumes no attenuation in the background. Then we inverted the same frequency groups as for the V_P, beginning from the 36 Hz. The final Q_p^{-1} solution from this effort, after inversion of the 128 Hz group, is shown in Figure 4c. The following aspects of the final Q_p^{-1} solution are notable. First, the attenuation updates have a strong lateral character. For example, the updates mainly occur between 5 m and 55 m model distance and 60 m and 75 m model distances indicating lateral heterogeneity in the source of attenuation. Therefore, we performed quantitative waveform comparison (Figure S2) to affirm that within the limits of the resolution the Q_P^{-1} solution is not plagued by artifacts, i.e., the features of this solution are required to replicate the recorded waveforms. Second, maximum attenuation updates mainly occur above the water table oscillation zone. We performed standard checkerboard resolution tests to understand the nature of the solutions (Figure S3). The resolution test show the following: a) the waveforms have a maximum vertical resolution of 4 m and a maximum horizontal

resolution also of 4 m, which is laterally better than the MASW solution but vertically poorer; b) the vertical smearing tends to over predict solutions closer to the surface.

A closer inspection of Figure 4c indicates that the maximum attenuation is occurring above the water-table oscillation zone and not within it. We believe it is a resolution issue and instead of interpreting the internal structure of every high attenuation patch, it is best to consider an averaged structure over a 4 m thickness interval for interpretation purposes. Figure 4c can be interpreted as indicating intermittent zones of low and high attenuation with the maximum attenuation as high as ~50-80%. This upper limit of attenuation in Figure 4c is comparable to those observed by Davis et al. (2010), Kwon and Ajo-Franklin (2013) and Noh et al. (2016) in their biofilm experiment. We speculate that, much like the V_S structure, the attenuation structure is also rooted in the water-table oscillation zone (although higher resolution data will be needed to prove this beyond doubt) and is reflective of the lateral distribution of the biomass. Unfortunately, our core is located at a high attenuation zone and we do not have sediment samples from non-attenuating parts of the profile to test this speculation.

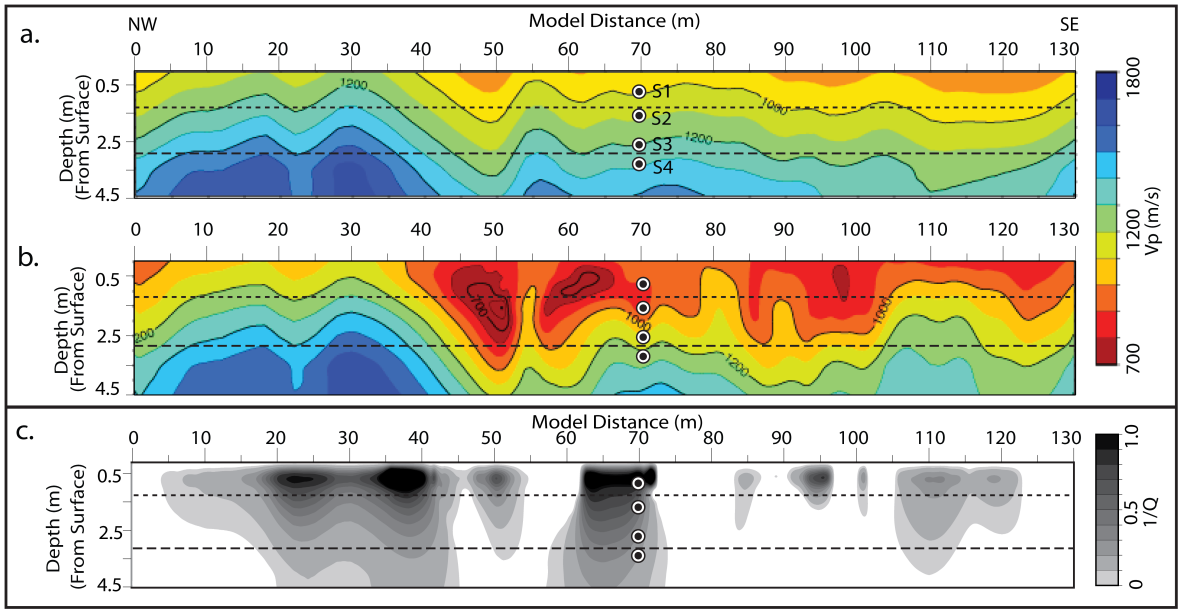

Figure 4 – a) Traveltime V_P solution, b) 124Hz Waveform V_P solution and c) 124Hz waveform Q_P^{-1} solution. In (a)- (c) solid black dots are ESEM samples locations.

Even if our speculation that both V_S and attenuation enhancement are caused primarily by biofilms, reconciling the V_S and attenuation solution is challenging. For example, at 80 m model distance, enhancement occurs in the V_S but not in attenuation. Two aspects of the attenuation solution need to be understood. First, it is relative. Our FWI begins by assuming a zero attenuation throughout the model. This however does not mean that the media is non-attenuative. The FWI merely adjusts a starting attenuation model minimally to fit the field data in the best possible manner. Second, that attenuation in itself is a very complex phenomenon (*Johnston et al., 1979*). In the context of biofilms, there may be a multitude of reasons that would affect attenuation. Biofilms have a complex internal structure with varying pore shapes and sizes as well as biofilm wall thickness (*Zhang et al., 1994*). Attenuation, which is very sensitive to subtle changes in sediment texture, is therefore expected to show more variations than propagation velocities.

A salient aspect of our result is that V_P perturbation from the biomass is not as much as the V_S perturbation. A physical explanation can be conceived using a simple mechanistic model that assumes the biomass as grain-coating cement. Assuming that the sediment grains are spherical and randomly distributed and the pores are fully connected, the bulk elastic moduli of the sediment mass for seismic frequencies can be formulated using physics-based models where the nominal procedure is to compute the elastic moduli of the drained sediments and pore-fluid separately and merge them using Gassmann's substitution. In our case, while formulating such a model we can assume that porosity and coordination number is high (40% and 9 respectively) but the key is to decide how to incorporate the biomass. Similar to the Jaiswal et al. (2014) study, if we base the grain arrangements as seen on the ESEM images (sample S2 and S3; Figure 3b), the biofilm should be incorporated as grain-coating and cementing medium. We have also assumed the Poisson's ratio of biofilm to be zero, implying it is a spongy material (*Jaiswal et al. 2014*).

Two end-member cement arrangements are possible as lower and upper bounds of the solution. In the first arrangement (upper bound), the cement is assumed to be accumulating at the grain contacts. In the second (lower bound), the cement is assumed to be uniformly coating the grains. From a modeling perspective, the main difference between the two arrangements is the change in ratio of the grain radius to radius of the cement layer (*Avset et al. 2009*); the former arrangement has a higher and the later arrangement has a lower ratio. Figure 5 shows changes in V_P and V_S with change in biomass cement for the two arrangements. The elastic parameters used to generate Figure 5 are presented in Table 1. With increasing biomass, both arrangements increase V_S and

V_p but the proportionate increase in V_S is higher. Using the lower bounds, we are able to replicate the Noh et al. (2016) observations, e.g., >50% increase in V_S at ~10% biofilm saturation. However, the cementation model also shows an increase in V_P which is not consistent with the experimental results. This is difficult to explain unless free gas (in bubble phase which reduces V_P leaving V_S largely unaffected) is also assumed to be present in the system or the internal porous structure of the biofilms are modulating the seismic waveform in ways that are not yet fully appreciated.

Assuming the lower bounds as a possible mechanistic arrangement at the Norman landfill site, the 60-50% increase in V_S suggested by our data will correspond to a biofilm saturation of ~4-5%. We recognize that this interpretation is overly simplistic unless overlapping signals from mineralization (e.g. S2), free gas, and change in the background lithology are independently determined. To the best of our knowledge, till date, no laboratory or field studies have encountered >100% increase in V_S at low biofilm saturation (4-10%) as predicted by the upper bound. The lower bound is probably reflective of the universal nature of the biofilm growth on sediment surfaces. A common threshold of 60-80% enhancement in Q_P^{-1} and 50% enhancement in V_S among many experiments globally also warrants explanation. Common sand packs used in laboratory tests as well as the sediments in the near-surface that are at near-critical porosity can only hold up to a maximum amount of biofilm which might result in comparable seismic signatures. However, this hypothesis needs to be tested by standardizing experimental procedures for microbial growth.

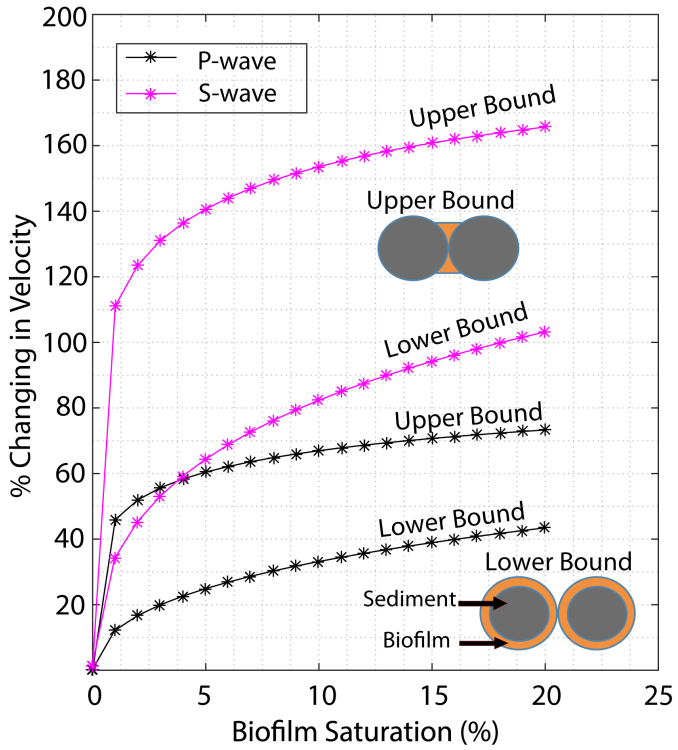

Figure 5 *– V_P and V_S versus biofilm saturation for a) biofilm cement at grain contacts (labeled upper bound) and b) biofilm cement coating the grains (labeled lower bound).*

Table 1: Rock physics modeling parameters.

Type of Material	Shear Modulus (GPa)	Poisson's Ratio	Density
Quartz	45	0.064	2.65
Biofilm	3	0 (sponge)	1.5

CHAPTER V

CONCLUSIONS

We have shown, for the first time, that biofilms can be detected *in-situ* in field settings using minimally invasive conventional surface seismic methods. Like peer laboratory studies, in sediments with biomass accumulation, we also observe significant enhancement in V_S and Q_P^{-1} but only subtle changes in V_P. Using a mechanistic model, where biofilms uniformly coat sediment grains we can explain how V_S should increase more rapidly compared to V_P in response to biomass growth. Biofilms have causative relationship with both V_S and Q_P^{-1}, therefore simultaneous acquisition of both P- and S-waves is advantageous. In the absence of independent horizontal-mode propagation recording, we generated V_S from ground roll. In our case, the V_S model had a better vertical resolution while the V_P model had a better horizontal resolution. In the field setting, V_S provides a more diagnostic tool for biofilm detection and monitoring. Many variations of our approach is possible, one where three-component sensors in a 3D grid record the same shot would be most informative. It is also easy to see that surface seismic techniques could be used in conjunction with other geophysical methods such as electrical and NMR to better image spatiotemporal biomass distribution in biogeochemical hot zones (such as hyporehic zone, contaminant plume fringe and

groundwater fluctuation zone), soil remediation, biobarriers, microbial enhanced oil recovery, and CO2 sequestration studies.

REFERENCES

Abdel Aal, G.Z., Atekwana, E.A., Atekwana, E.A., 2010. Effect of bioclogging in porous media on complex conductivity signatures. J. Geophys. Res. 115, 1–10. doi:10.1029/2009JG001159

Ahimou, F., Semmens, M.J., Novak, P.J., Haugstad, G., 2007. Biofilm cohesiveness measurement using a novel atomic force microscopy methodology. Appl. Environ. Microbiol. 73, 2897–2904. doi:10.1128/AEM.02388-06

Atekwana, E., Mewafy, F., 2014. High-resolution magnetic susceptibility measurements for investigating magnetic mineral formation during microbial mediated iron reduction. J. Geophys. Res. Biogeosciences 1–15. doi:10.1002/2013JG002414.Received

Avseth, P., Mukerji, T., Mavko, G., 2009. Quantitative Seismic Interpretation, Cambridge University Press. doi:10.1017/CBO9781107415324.004

Baveye, P., Vandevivere, P., Hoyle, B.L., DeLeo, P.C., de Lozada, D.S., 1998. Environmental Impact and Mechanisms of the Biological Clogging of Saturated Soils and Aquifer Materials. Crit. Rev. Environ. Sci. Technol. 28, 123–191. doi:10.1080/10643389891254197

Borch, T., Kretzschmar, R., Skappler, A., Van Cappellen, P., Ginder-Vogel, M., Voegelin, A.,

Campbell, K., 2010. Biogeochemical redox processes and their impact on contaminant dynamics. Environ. Sci. Technol. 44, 15–23. doi:10.1021/es9026248

Brenders, A.J., Pratt, R.G., 2007. Full waveform tomography for lithospheric imaging: Results from a blind test in a realistic crustal model. Geophys. J. Int. 168, 133–151. doi:10.1111/j.1365-246X.2006.03156.x

Brovelli, A., Malaguerra, F., Barry, D. a., 2009. Bioclogging in porous media: Model development and sensitivity to initial conditions. Environ. Model. Softw. 24, 611–626. doi:10.1016/j.envsoft.2008.10.001

Bunks, C., 1995. Multiscale seismic waveform inversion. Geophysics 60, 1457. doi:10.1190/1.1443880

Collins, K.L., 2001. Permeability pathways in the Canadian River alluvium adjacent to the Norman Landfill.

Cozzarelli, I.M., Böhlke, J.K., Masoner, J., Breit, G.N., Lorah, M.M., Tuttle, M.L.W., Jaeschke, J.B., 2011. Biogeochemical evolution of a landfill leachate plume, Norman, Oklahoma. Ground Water 49, 663–687. doi:10.1111/j.1745-6584.2010.00792.x

Cozzarelli, I.M., Suflita, J.M., Ulrich, G. a., Harris, S.H., Scholl, M. a., Schlottmann, J.L.,

Christenson, S., 2000. Geochemical and microbiological methods for evaluating anaerobic processes in an aquifer contaminated by landfill leachate. Environ. Sci. Technol. 34, 4025–4033. doi:10.1021/es991342b

Cunningham, A., 1991. Influence of biofilm accumulation on porous media hydrodynamics. … Sci. Technol. 1305–1311. doi:10.1021/es00019a013

Davis, C. a., Pyrak-Nolte, L.J., Atekwana, E. a., Werkema, D.D., Haugen, M.E., 2010. Acoustic and electrical property changes due to microbial growth and biofilm formation in porous media. J. Geophys. Res. 115, 1–14. doi:10.1029/2009JG001143

DeJong, J.T., Fritzges, M.B., Nüsslein, K., 2006. Microbially Induced Cementation to Control Sand Response to Undrained Shear. J. Geotech. Geoenvironmental Eng. 132, 1381–1392. doi:10.1061/(ASCE)1090-0241(2006)132:11(1381)

Donald W. Marquardt, 1963. An Algorithm for Least-Squares Estimation of Nonlinear. J. Soc. Ind. Appl. Math. 11, 431–441.

Gardner, G.H.F., Gardner, L.W., Gregory, A.R., 1974. Formation Velocity and Density - The Diagnostic Basics for Stratigraphic Traps. Geophysics 39, 770–780.

Hand, V.L., Lloyd, J.R., Vaughan, D.J., Wilkins, M.J., Boult, S., 2008. Experimental studies of the influence of grain size, oxygen availability and organic carbon availability on bioclogging in porous media. Environ. Sci. Technol. 42, 1485–1491. doi:10.1021/es072022s

Hole, J.A., Zelt, C.A., 1995. Finite-Difference Reflection Traveltimes. Geophys. J. Int. 427–434.

Jaiswal, P., Al-Hadrami, F., Atekwana, E.A., Atekwana, E.A., 2014. Mechanistic models of biofilm growth in porous media. J. Geophys. Res. Biogeosciences 119, 557–566. doi:10.1002/2013JG002433

Jo, C., Shin, C., Suh, J.H., 1996. 2-D scalar wave extrapolator. Geophysics 61, 529–537.

Johnston, D. H., Toksöz, M. N., & Timur, A. (1979). Attenuation of seismic waves in dry and saturated rocks: II. Mechanisms. Geophysics,44(4), 691-711.

Kao, C.M., Chen, S.C., Liu, J.K., 2001. Development of a biobarrier for the remediation of PCE-contaminated aquifer. Chemosphere 43, 1071–1078. doi:10.1016/S0045-6535(00)00190-9

Kasi, M., McEvoy, J., Padmanabhan, G., Khan, E., 2011. Groundwater remediation using an enricher reactor-permeable reactive biobarrier for periodically absent contaminants. Water Environ. Res. 83, 603–12. doi:10.2175/106143011X12928814444457

Kirkland, C.M., Herrling, M.P., Hiebert, R., Bender, A.T., Grunewald, E.D., Walsh, D.O., Codd, S.L., 2015. In-situ detection of subsurface biofilm using low-field NMR-a field study. Environ. Sci. Technol. doi:10.1021/acs.est.5b02690 30

Klapper, I., Rupp, C.J., Cargo, R., Purvedorj, B., Stoodley, P., 2002. Viscoelastic fluid description of bacterial biofilm material properties. Biotechnol. Bioeng. 80, 289–296. doi:10.1002/bit.10376

Kwon, T., Ajo-franklin, J.B., 2013. High-frequency seismic response during permeability reduction due to biopolymer clogging in unconsolidated porous media. Geophysics 78, EN117-EN127. doi:doi:10.1190/geo2012-0392.1

Lazar, I., Petrisor, I.G., Yen, T.F., 1989. Microbial Enhanced Oil Recovery. Dev. Pet. Sci. 22, 125–149. doi:10.1016/S0376-7361(09)70095-0

Masoner, J.R., Cozzarelli, I.M., 2015. Spatial and temporal migration of a landfill leachate plume in alluvium. Water. Air. Soil Pollut. 226. doi:10.1007/s11270-014-2261-x

Mitchell, A.C., Dideriksen, K., Spangler, L.H., Cunningham, A.B., Gerlach, R., 2010. Microbially enhanced carbon capture and storage by mineral-trapping and solubility-trapping. Environ. Sci. Technol. 44, 5270–5276. doi:10.1021/es903270w

Noh, D., Ajo-franklin, J.B., Kwon, T., Muhunthan, B., 2016. P and S wave responses of bacterial biopolymer formation in unconsolidated porous media 1–20. doi:10.1002/2015JG003118.Received

Ntarlagiannis, D., Ferguson, A., 2009. SIP response of artificial biofilms. Geophysics 74, 1–5. doi:10.1190/1.3031514

Pratt, R.G., 1999. Seismic waveform inversion in the frequency domain, Part 1: Theory and verification in a physical scale model. Geophysics 64, 888. doi:10.1190/1.1444597

Rijal, M.L., Appel, E., Petrovsk., E., Blaha, U., 2010. Change of magnetic properties due to fluctuations of hydrocarbon contaminated groundwater in unconsolidated sediments. Environ.

Pollut. 158, 1756–62. doi:10.1016/j.envpol.2009.11.012

Scholl, M.A., Cozzarelli, I.M., Christenson, S.C., 2006. Recharge processes drive sulfate reduction in an alluvial aquifer contaminated with landfill leachate. J. Contam. Hydrol. 86, 239–261. doi:10.1016/j.jconhyd.2006.03.005

Seifert, D., Engesgaard, P., 2012. Sand box experiments with bioclogging of porous media: Hydraulic conductivity reductions. J. Contam. Hydrol. 136–137, 1–9. doi:10.1016/j.jconhyd.2012.04.007

Stegen, J.C., Fredrickson, J.K., Wilkins, M.J., Konopka, A.E., Nelson, W.C., Arntzen, E. V,

Chrisler, W.B., Chu, R.K., Danczak, R.E., Fansler, S.J., Kennedy, D.W., Resch, C.T., Tfaily, M., 2016. Groundwater–surface water mixing shifts ecological assembly processes and stimulates organic carbon turnover. Nat. Commun. 7, 11237. doi:10.1038/ncomms11237

Stoodley, P., Lewandowski, Z., Boyle, J.D., Lappin-Scott, H.M., 1999. Structural deformation of bacterial biofilms caused by short-term fluctuations in fluid shear: An in situ investigation of biofilm rheology. Biotechnol. Bioeng. 65, 83–92. doi:10.1002/(SICI)1097-0290(19991005)65:1<83::AID-BIT10>3.0.CO;2-B

Totsche, K.U., Rennert, T., Gerzabek, M.H., Kögel-Knabner, I., Smalla, K., Spiteller, M., Vogel, H.J., 2010. Biogeochemical interfaces in soil: The interdisciplinary challenge for soil science. J. Plant Nutr. Soil Sci. 173, 88–99. doi:10.1002/jpln.200900105

Tsuneda, S., Aikawa, H., Hayashi, H., Yuasa, A., Hirata, A., 2003. Extracellular polymeric substances responsible for bacterial adhesion onto solid surface. FEMS Microbiol. Lett. 223, 287–292. doi:10.1016/S0378-1097(03)00399-9

Vandevivere, P., Baveye, P., de Lozada, D.S., DeLeo, P., 1995. Microbial Clogging of Saturated Soils and Aquifer Materials: Evaluation of Mathematical Models. Water Resour. Res. 31, 2173–2180. doi:10.1029/95WR01568

Vidale, J., 1988. Finite-difference calculation of travel times. Bull. Seismol. Soc. Am. 78, 2062–2076.

Xia, J., Miller, R.D., Park, C.B., 1999. Estimation of near-surface shear-wave velocity by inversion of Rayleigh waves. Geophysics 64, 691. doi:10.1190/1.1444578

Zhang, T. C., & Bishop, P. L. (1994). Structure, activity and composition of biofilms. Water Science and Technology, 29(7), 335-344

Zhang, C., Revil, A., Fujita, Y., Munakata-Marr, J., Redden, G., 2014. Quadrature conductivity: A quantitative indicator of bacterial abundance in porous media. Geophysics 79, D363–D375. doi:10.1190/geo2014-0107

APPENDICES

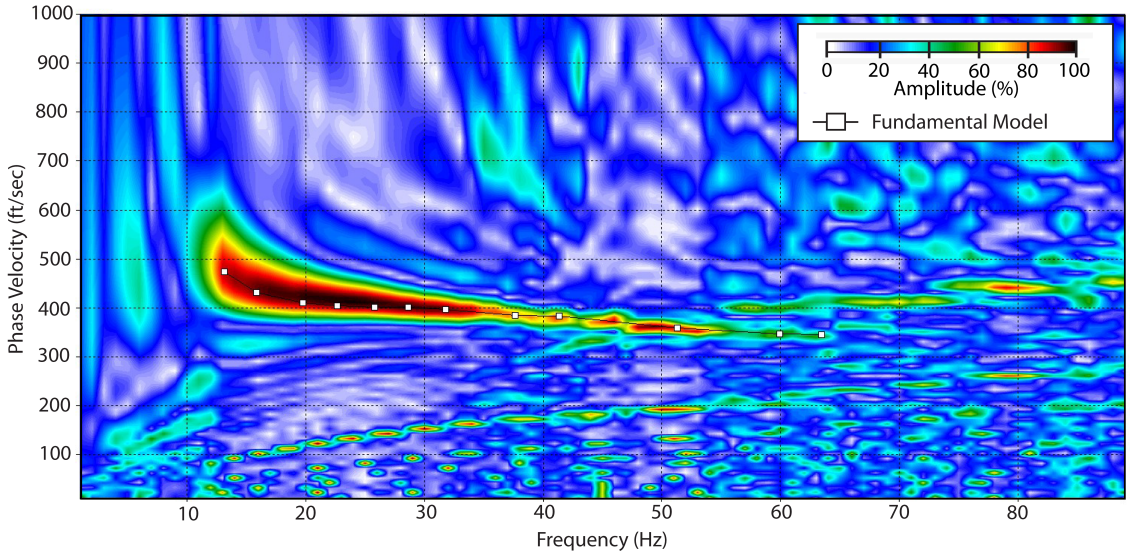

Figure S1 – Dispersion curve image of the 10-geophone receiver spread showing strong fundamental mode characteristics.

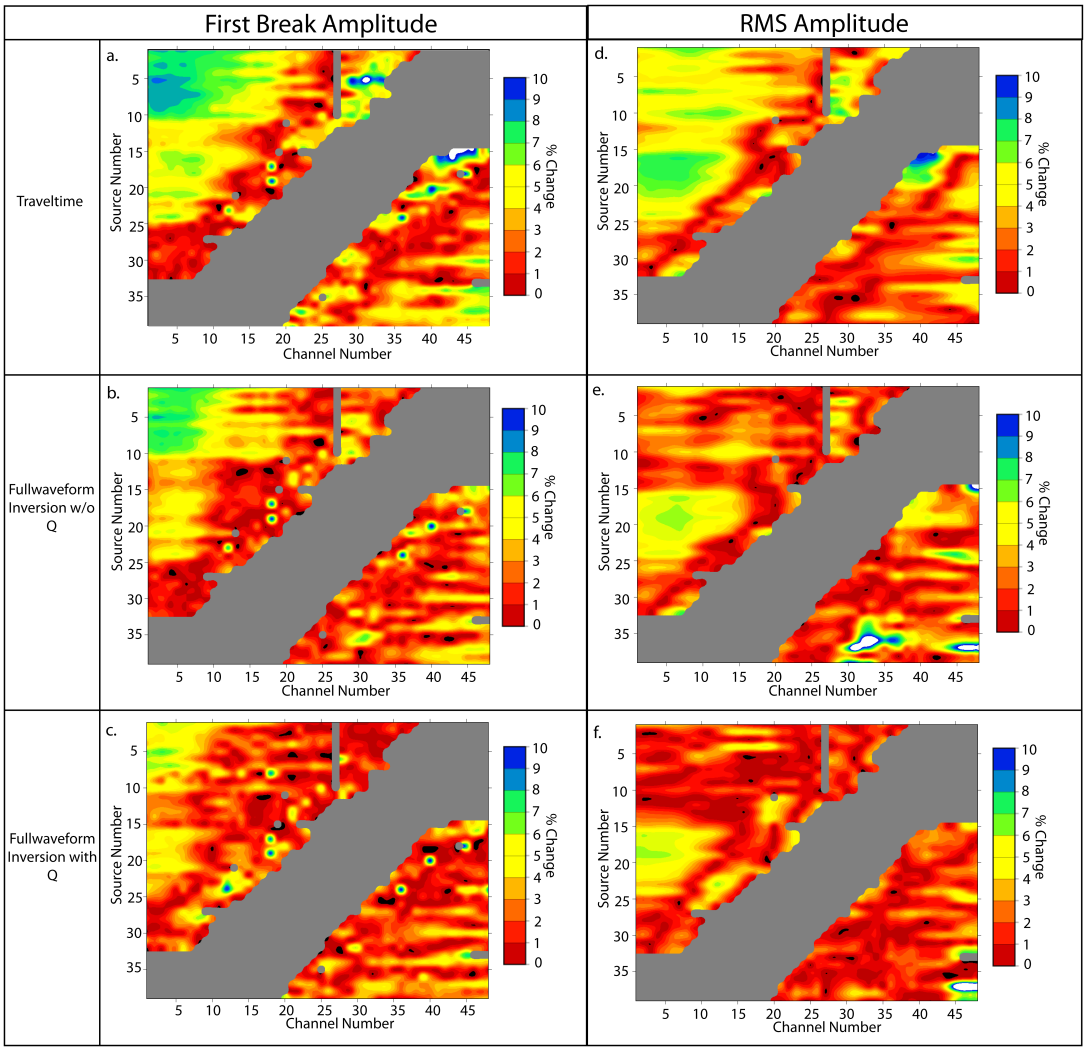

Figure S2 – Amplitude error plots for synthetic data obtained from final traveltime, waveform inversion without Q_p^{-1} and waveform inversion with Q_p^{-1} models. The error was calculated relative to the real data using the following formula: $[E_{REAL}-E_{CALC}/E_{REAL}]*100$. a), b) and c) show error plots for traveltime, waveform without Q_p^{-1} and waveform with Q_p^{-1} first break amplitude, respectively. d), e) and f) show error plots for traveltime, waveform without Q_p^{-1} and waveform with Q_p^{-1} RMS amplitude. It is clear that waveform with Q_p^{-1} fits the real data pretty well for the RMS amplitude.

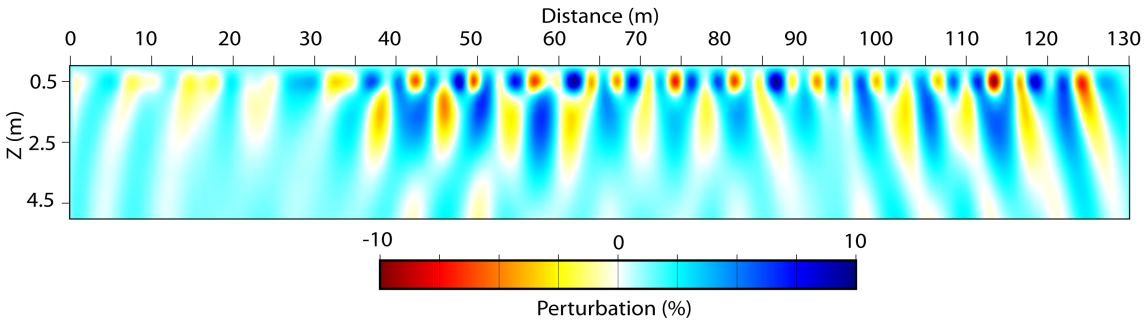

Figure S3 – Checkerboard resolution test for velocity perturbation for FWI.

VITA

Sundeep Sharma

Candidate for the Degree of

Master of Science

Thesis: IN-SITU FIELD BIOFILM DETECTION USING SEISMIC METHODS

Major Field: Geology

Biographical:

Education:

Completed the requirements for the Master of Science/Arts in Geology at Oklahoma State University, Stillwater, Oklahoma in December, 2016.

Completed the requirements for the Master of Science/Arts in Environmental Geology/Geophysics at Rutgers University, Newark, New Jersey in May, 2014.

Completed the requirements for the Bachelor of Science/Arts in your major at New Jersey Institute of Technology, Newark, New Jersey in May, 2012.

Experience:

- Geophysics Intern – Devon Energy, Oklahoma City,OK : Summer 2016
- Teaching and Research Assistant – Oklahoma State University, Stillwater, OK: August 2014 – May 2016
- Independent Researcher – U.S. Environmental Protection Agency: March 2013 – February 2014
- Research /Field Assistant – Rutgers University, Newark, NJ : December 2011 – May 2012

Professional Memberships:

- Society of Exploration Geophysicist
- European Association of Geoscientists and Engineers
- Environmental and Engineering Geophysical Society